Title	Improved performance of strain sensors constructed from highly crystalline graphene with nanospacer
Author(s)	Xu, Zizhao; Himura, Yuna; Ishiguro, Chikako et al.
Citation	Japanese Journal of Applied Physics. 2023, 63(1), p. 015001
Version Type	AO
URL	https://hdl.handle.net/11094/93340
rights	
Note	

Improved performance of strain sensors constructed by highly crystalline graphene with nanospacer

Zizhao Xu[1*], Yuna Himura[1], Chikako Ishiguro[1], Taiki Inoue[1], Yuta Nishina[2], Yoshihiro Kobayashi[1*]

[1]*Department of Applied Physics, Graduate School of Engineering, Osaka University, 2-1 Yamadaoka, Suita, Osaka, 565-0871, Japan*

[2]*Research Core for Interdisciplinary Sciences, Okayama University, 3-1-1 Tsushima-naka, Kita-ku, Okayama, 700-8530, Japan*

Email addresses: zizhao_xu@ap.eng.osaka-u.ac.jp, kobayashi@ap.eng.osaka-u.ac.jp

Abstract

Graphene shows promise as an alternative material for strain sensors, due to its excellent properties, which can overcome the limitations of conventional metal ones. However, current graphene-based strain sensors were fabricated from chemically reduced graphene oxide (rGO) and suffered from low linearity and large hysteresis in sensor response as well as high initial resistance. These issues should be caused by functional groups and defects remaining on the rGO. Herein, highly crystalline rGO is employed for the fabrication of the strain sensor. The porous rGO sponge with low defect density is prepared in bulk scale via the ethanol-associated thermal process at ultra-high temperature. The obtained rGO sensor exhibits improved linearity, low initial resistance, and very small hysteresis owing to the high crystallinity of the rGO. Composite of rGO with nano-diamond, which has a role as nanospacer to separate the rGO layers, is found to be very effective to enhance the sensitivity.

1. Introduction

Strain sensors are devices aiming to convert changes in length into resistance signals[1], which are being explored in various potential applications such as automated logistics transportation[2], autonomous driving[3], and human motion monitoring[4, 5]. The conventional strain sensors obtain resistance signals through a mechanism that involves resistance increase achieved by reducing the cross-sectional area of the internal metal wire when stretching. However, this mechanism results in low sensitivity and insufficient operating range[6-8], making them incapable of meeting the demands of the applications in the future. Researchers have studied nanomaterials as strain sensor material[9], including graphene[10-12], carbon black particles[13, 14], metal nanostructures[15, 16], and polymer nanofibers[17]. Unlike the metal wire with low stretchability in conventional stain sensors, nanomaterials offer high stretchablity[18, 19] since they exist as individual components which can be easily separated, addressing the issue of a narrow operating range. Notably, graphene-based material[10-12] was supposed to be an ideal candidate for strain sensors due to the excellent properties of monolayer graphene, such as mechanical strength, surface area, and electric conductivity[20].

However, the recently reported graphene-based strain sensors suffer from some issues, including low linearity[21, 22], large hysteresis[23], and high initial resistance[24, 25], which restrict their practical application[26]. These issues arise due to the requirement of bulk-scale graphene in the fabrication of strain sensors. Typically bulk-scale graphene is produced through the reduction of graphene oxide (GO), where reducing chemical agents or hydrothermal treatment in an autoclave was employed. The graphene fabrication by chemical reduction of GO introduces the inevitable problems of the high defect density and functional group remaining on the prepared reduced GO (rGO)[27], which can result in the mentioned issues. The low linearity, the most serious issue, should be attributed to the remaining functional groups[22, 26], because they provide

undesirable cross-linking between rGO flakes[28]. The sensor response is evaluated by variation of electrical resistance for rGO samples and is dominated by the contact area between the rGO flakes in the sensor device. The cross-linking should cause non-linear deformation of rGO flakes on the strain sensor operation, leading to poor linearity in the sensor response of the relation between the resistance and device length. The large hysteresis, the second serious issue, should be due to the low mechanical strength, originating from the high defect density in the rGO [20, 29]. The low mechanical strength of rGO flakes leads to inefficient stress transmission on rGO flake[6, 30]. This deviation from elastic deformation causes fluctuations in the contact area between rGO flakes during strain sensor operation. Accordingly, the resistance incompletely responds to deformation, and larger hysteresis should be observed from strain sensors with rGO with low crystallinity. The high initial resistance, the third serious issue, is also caused by the high defect density of rGO[31, 32], which is the resistance of strain sensor without deformation. Therefore, a higher applied voltage is required for strain sensing, as strain sensors are typically read by measuring the current at a constant voltage. Accordingly, the issues of low linearity, large hysteresis, and high initial resistance can be solved by utilizing highly crystalline rGO with low defect density and a reduced number of functional groups. Bulk-scale rGO with high crystallinity can be obtained through our previous study[33, 34], including freeze-drying and ethanol-associated ultra-high temperature process. Additionally, the random-stacking structure of rGO can also be achieved and is expected to exhibit high conductivity due to reduced interaction between rGO layers compared with AB-stacked graphene[35, 36]. It has been proved that the randomly stacked structure of rGO can achieve excellent properties similar to those of monolayer graphene, surpassing those of the AB-stacked structure[35, 36].

Moreover, we propose a novel strategy to further enhance the sensitivity. Compared to conventional metal-based strain sensors, rGO exists as individual flakes in graphene-

based strain sensor, which can effectively separate by stretching operation. To further reduce the interaction between rGO flakes and enhance the sensor sensitivity, nano-diamonds (NDs) were added as a nanospacer between rGO flakes to physically prevent stacking and effectively separate the rGO flakes during the sensor operation. The ND is made up of an inner layer of a cubic diamond crystal (sp^3-hybridization) and a surface layer of oxygen-containing groups[37, 38]. Notably, while graphene is a two-dimensional (2D) material, ND is a zero-dimension (0D) material. The ND is transformed into carbon nano-onion (CNO)[39] by thermal treatment at more than 1000 °C, which can facilitate the separation of rGO flakes[40, 41]. It should be noted that the CNO can form a conductive path for current in sensor devices since it is composed of sp^2-hybridization and is highly conductive[42]. This combination of graphene and the ND forms resilient 2D/0D mixed-dimensional heterostructures, effectively reducing the contact area between rGO flakes and yielding a higher resistance difference during sensor operation. Accordingly, the composite of rGO with ND as nanospacer was examined in this study for promising material to enhance the sensitivity of strain sensors.

In this study, to achieve low linearity, large hysteresis, and high initial resistance in graphene-based strain sensor, we used the freeze-drying and the ethanol-associated ultra-high temperature process to improve the crystallinity of rGO. Moreover, to ameliorate the sensitivity of the strain sensor, we investigated the effect of ND addition on reducing the interaction between rGO flakes. Also, we constructed a model to understand the unexpected trends of the resistance of strain sensor with increasing ND concentration. The strain sensor possessing high linearity, high sensitivity, and low initial resistance will pave the way for utilization, such as human motion detection and automated logistics transportation.

2. Experimental

Figure 1 shows the fabrication process of strain sensors from rGO. GO dispersion (1 wt%) was prepared using a modified Hummers' method[43]. The size of the GO flakes was measured to be approximately 10 μm by optical microscopy. The NDs were prepared using the detonation method, which had an average diameter of 5 nm by an atomic force microscopy. The water dispersion of NDs with 1 wt% was applied as received from Nippon Kayaku Co. The sponges of GO and GO/ND were prepared by blending and freeze-drying as stated in our former research[34].
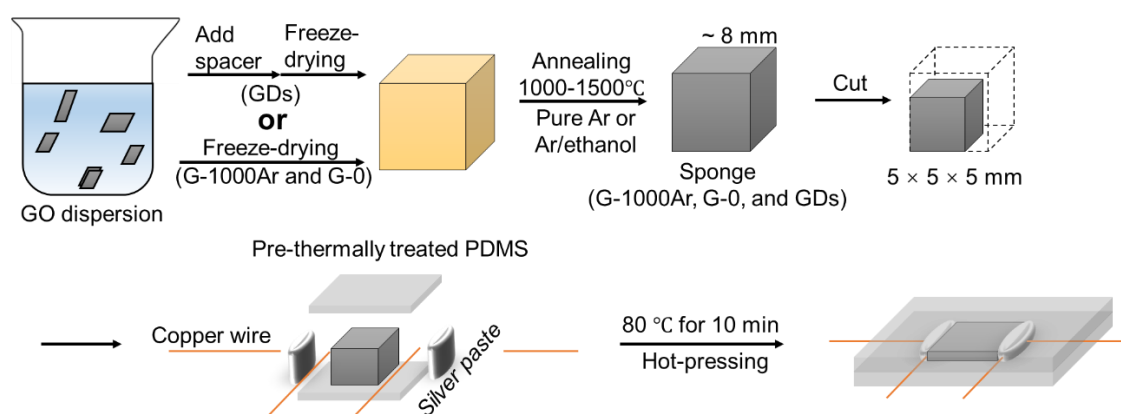
Fig. 1. Process of rGO strain sensor preparation

The GO and composite sponges were reduced and repaired under ultra-high temperature conditions with pure Ar or ethanol/Ar[33, 34]. We used a tubular electric furnace (HT1500-50-32P, HEAT TECH Co.) to conduct the ultra-high temperature process at 1000 °C or 1500 °C, with a vacuum pump keeping the chamber at low pressure. The rGO sample was prepared from GO sponge without ND under the condition with pure Ar at 1000 °C and with ethanol/Ar at 1500 °C, named as G-1000Ar and G-0, respectively. The GO/ND sponge samples were treated at 1500 °C with ethanol/Ar, and are named as GD-1, GD-2, GD-3, GD-4, and GD-5 according to the

concentration of mixed ND for 0.01 wt%, 0.02 wt%, 0.05 wt%, 0.1 wt%, and 0.2 wt%, respectively. The series of the samples is also called GDs.

To prepare a strain sensor, the obtained G-1000Ar, G-0, and GDs sponges were cut into 5 mm ×5 mm ×5 mm cubes. The dimethylsiloxane was mixed with the initiator. This mixture was poured into the mold and heated at 80 °C for 7 min, and the partially polymerized polydimethylsiloxane (PDMS) film was obtained with about 35 mm ×25 mm ×2 mm. The cut sponge(G-1000Ar, G-0, or GDs), silver paste, and copper wire were placed on the PDMS film, and covered with another PDMS film, as shown in Fig. 1. By applying pressure and further heat treatment (66 kPa and 80 °C for 10 min), strain sensors were obtained to be ready for the operation.

Raman spectra were obtained by LabRAM HR-800 UV (Horiba Jobin Yvon) with a 532 nm wavelength for the excitation laser, 1 mW power, and ~0.7 μm of spot size. All the Raman results are obtained by averaging the data measured from 20 random spots. The sensor performance was tested with a lab-made measuring device, as shown in Fig. S1. The device consisted of two parts: the sensor operation part and the resistance measurement part. The sensor operation part consisted mainly of a stepping motor and its control unit, while the resistance measurement part was implemented by a DC voltage-current source/monitor (ADC 6241A). The contact resistance was evaluated by comparing the initial resistance of GDs obtained using both the 2-wire and 4-wire methods, as well as the comparison of sensor performance of G-0 evaluated separately using both methods, as shown in Fig. S2. It should be noted that the 2-wire method was exclusively used for this evaluation, whereas the 4-wire method was employed for all other samples to ensure accurate measurements by minimizing the influence of contact resistance between the wires and the strain sensor. Measured parameters to evaluate the sensor performance are denoted as follows. L_0 and R_0 are the initial length and resistance of a sponge sample without deformation, and ΔL and ΔR are the difference

of the length and the resistance between initial and operating conditions, respectively. $\Delta L/L_0$ and $\Delta R/R_0$ are the relative variation of length and resistance and were utilized for the evaluation of the sensor performance. Before the stretching process, R_0 was measured. In the stretching process, the sample was stretched up to 40% of $\Delta L/L_0$. The stretching process had five steps. Each step consists of 8% stretching in length ($\Delta L/L_0$), pausing for 2 s to stabilize possible delay of the deformation, and measurement of the resistance for strain sensing. After five steps of the stretching processes were completed, the sensor was operated to reverse direction for releasing the strain with the same step interval as the stretching process. The resistance at each step in the releasing process was measured and compared with the resistance for the stretching process to evaluate the hysteresis in the sensor operation. Thus, ΔR of each step can be obtained, and the ΔR_{max} was measured at the maximum of the $\Delta L/L_0$ (40%). The stretching and releasing processes were repeated ten times to obtain the averaged $\Delta R/R_0$. In this study, the sensitivity of the strain sensor is evaluated by gauge factor (GF), which is defined as GF = $(\Delta R/R_0)/(\Delta L/L_0)$. The linearity is obtained by the adjusted coefficient of determination of the linear regression of GF. The adjusted coefficient of determination is a statistical metric used to evaluate the accuracy of a model. In the strain sensor operation, proportional relationship between $\Delta R/R_0$ and $\Delta L/L_0$ indicates the sensor response with high linearity, which corresponds to improved accuracy of the measured value.

3. Result and discussion

To confirm the impact of rGO crystallinity on sensor performance, rGO samples of G-1000Ar and G-0 prepared by the thermal process at 1000 °C and 1500 °C were examined. No spacer material was incorporated in these samples for simplicity. The Raman spectra of G-0[34] and G-1000Ar had been measured for the evaluation of

crystallinity, as indicated in Fig. 2(a). The intensity ratio of the D-band to the G-band I(D)/I(G) corresponded to the defect density in graphene[44]. Fig. 2 (b) and (c) showed the observed sensor response from these samples, and the R_0 and the analyzed GF were plotted in Fig.2(d).
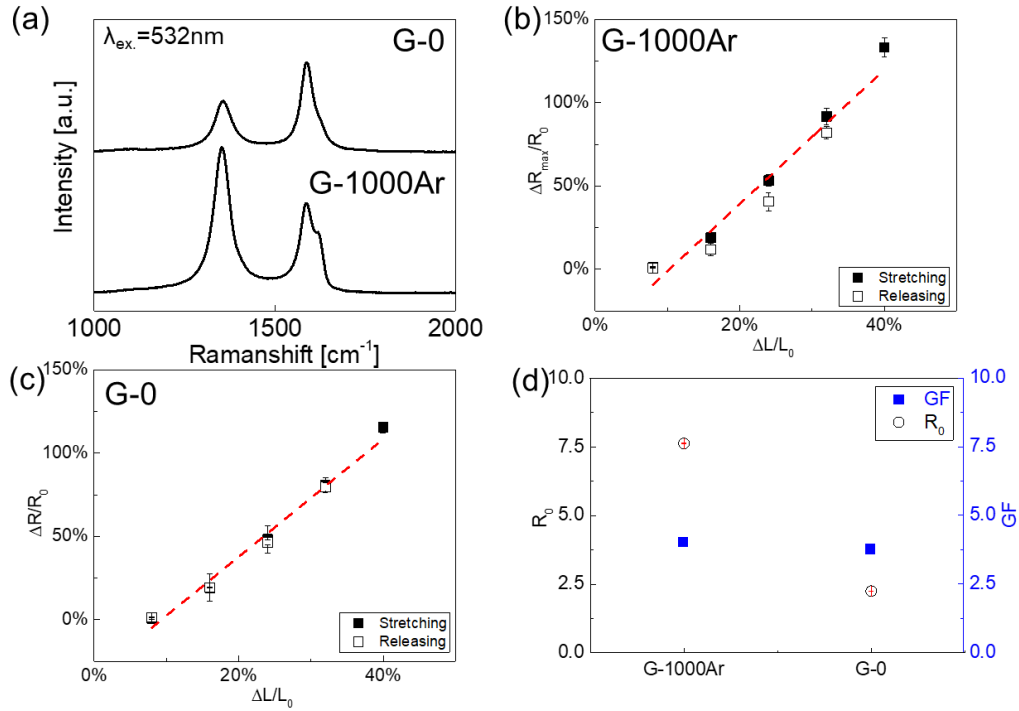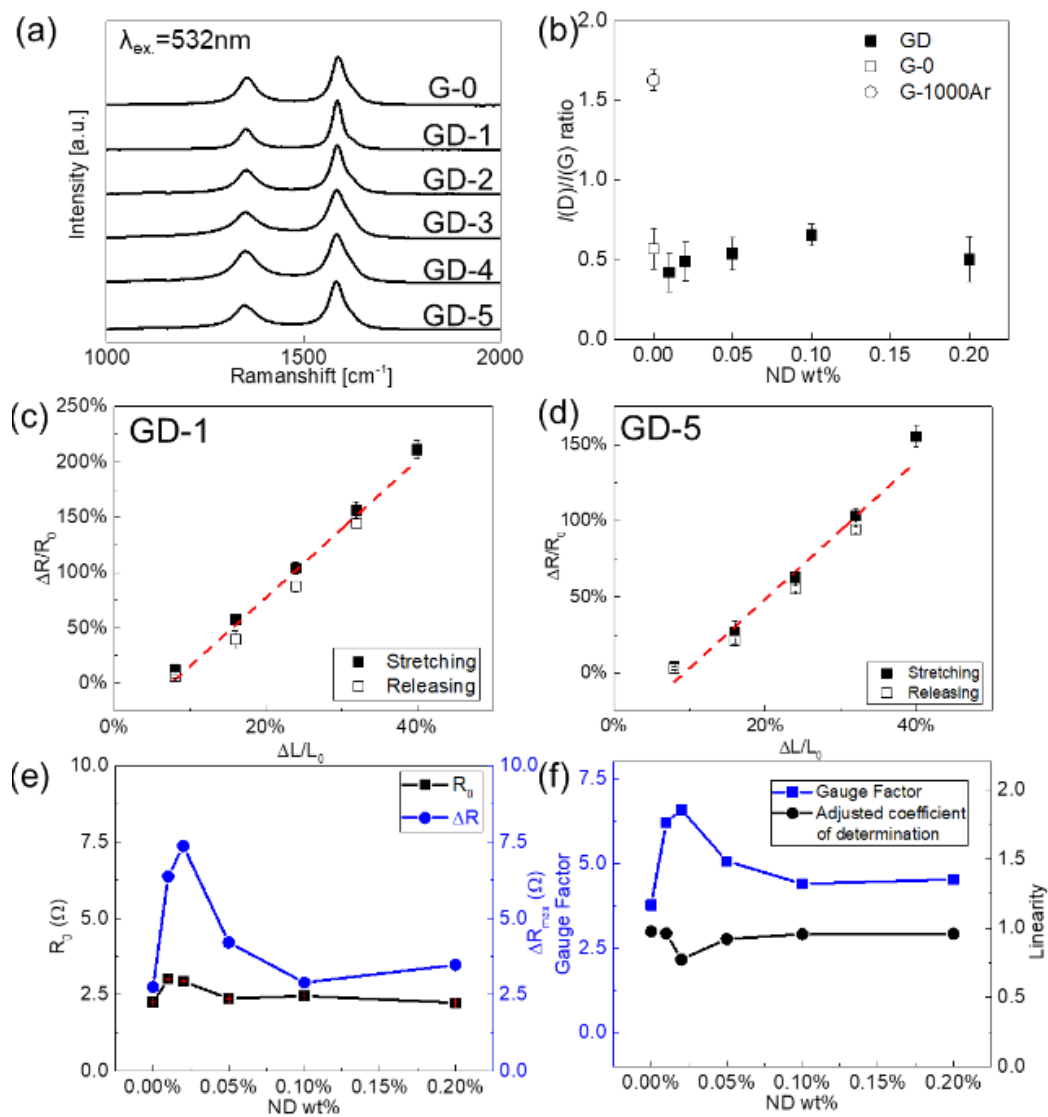

Fig. 2. (a) Raman spectra of G-1000Ar and G-0. Sensor operation of (b) G-1000Ar and (c) G-0 during the sensor operation process. (d) R_0 and GF of G-1000Ar and G-0.

Much lower I(D)/I(G) was observed from G-0 compared with G-1000Ar, indicating a lower defect density of G-0, where stronger mechanical strength should be expected due to high crystallinity. The D′-band observed at 1620 cm^{-1} for G-1000Ar also indicates a high defect density[45]. As for the linearity of the sensor response, both G-0 and G-1000Ar were observed to exhibit higher linearity compared with the previous reports[23]. This response preferable for sensor operation might be originated from the thermal process at high temperature, which causes the improved crystallinity and the

removal of the functional groups, resulting in the reduction of cross-linking between rGO layers. Relatively small hysteresis was observed from both G-1000Ar and G-0, as seen in Fig. 2 (b) and (c). A closer inspection of the differences revealed that G-1000Ar showed slightly larger hysteresis than that of G-0. This might be due to the decreased mechanical strength[20, 29] caused by the lower crystallinity for G-1000Ar, which shows higher $I(D)/I(G)$ in the Raman spectrum. The rGO flakes with higher defect density could not perfectly follow the strain during the sensor operation because of the unstable connection of rGO layers. Hence, slight hysteresis of the resistance was observed from G-1000Ar. On the other hand, G-0 exhibited higher crystallinity due to the ethanol-associated ultra-high temperature process and is expected to provide higher mechanical strength. Accordingly, the rGO flakes with lower defect density could be deformed elastically, and the connection of the rGO flake should be stable and similar for the stretching and releasing operation of the sensor. Hence, smaller hysteresis of the resistance was observed from G-0. Higher crystallinity also affected the initial resistance R_0 significantly. As shown in Fig. 2 (d), R_0 decreased from 7.70 Ω for G-1000Ar to 2.25 Ω for G-0, indicating improved conductance of rGO with lower defect density. The sensitivity of the strain sensor was evaluated by GF, which was obtained by the analysis of $\Delta R/R_0$ and $\Delta L/L_0$. Contrary to expectation, as shown in Fig. 2 (d), GF of G-0 was a similar value (~3.7) to that of G-1000Ar in spite of the large difference of their crystallinity and significant decrease of R_0 for G-0. This unexpected result might be caused by coordinated variation of ΔR and R_0, suggesting that the ΔR should be enlarged for achieving higher sensitivity.

As achieved for G-0, better linearity, smaller hysteresis, and lower R_0 will be expected for samples with higher crystallinity. Therefore, the condition of 1500 °C and Ar/ethanol gas was employed in the following study. In order to enhance ΔR during

sensor operation and the sensitivity (GF), we attempted to improve the separation of rGO flakes by reducing their interaction with the addition of ND.

Fig. 3. (a) Raman spectra of GDs and G-0. (b) $I(D)/I(G)$ ratio of G-1000Ar, G-0, and GDs. Sensor operation of (c) GD-1 and (d) GD-5 during the stretching and releasing process. (e) R_0 and ΔR against spacer concentration. (f) GF and linearity against spacer concentration.

Composite of rGO and various concentrations of ND was fabricated in the sponge form and was used for sensor operation after structural analysis by Raman spectroscopy.

The Raman spectra and their $I(D)/I(G)$ analysis for G-0 and GDs samples were already reported in our former work[34] and were shown again as Fig 3 (a) and (b). The Raman result showed that the $I(D)/I(G)$ ratios of the GDs samples ranged between 0.42–0.65, which were close to that of G-0 and lower than that of G-1000Ar. This means that the defect density of GDs and G-0 are quite comparable. The relationship between $\Delta R/R_0$ and $\Delta L/L_0$ evaluated during the sensor operation was indicated in Fig. 3 (c) and (d) for GD-1 and GD-5, and in Fig. S2 for GD-2, GD-3, and GD-4. As indicated in Fig. 3 (e), the R_0 values from G-0 and GDs were almost constant and did not virtually depend on the ND concentration, ranging between 2.23–3.02 Ω. On the other hand, the ΔR_{max} increased from 2.75 to 7.37 Ω by adding a relatively lower concentration of ND (0.01–0.02 wt%), and then decreased to about 3.47 Ω by adding a relatively higher concentration of ND more than 0.02 wt%. The dependence of the linearity and GF on ND concentration were plotted in Fig. 3 (f), where high linearity ranging mostly between 0.92 to 0.98 was observed for G-0 and GDs. The hysteresis for $\Delta R/R_0$–$\Delta L/L_0$ relationship in stretching and releasing operation was negligibly small for GDs, indicating that structural deformation by the stretching and releasing process should be very stable. Unusual behavior of GF was observed for the increase of ND concentration. The GF suddenly increased from 3.8 (G-0) to 6.6 (GD-1) by adding a small amount of ND. The increase of GF, however, became maximum at 0.01 wt% of ND (GD-1), and the GF gradually decreased to 4.4 by adding a higher concentration of ND. As summarized in Fig. S3, the sensor performance obtained from GD-1 surpassed that of the reported value in previous studies.

For the sensor performances with different ND concentrations, the R_0 showed similar values regardless of ND addition, while the ΔR_{max} first reached the peak after adding ND and subsequently decreased with increasing ND concentration (Fig. 3 (e)). To understand the trends of the R_0 and the ΔR_{max} observed in our experiment, we

constructed a model that simplifies the structure of the rGO sponge. In this model, the resistance of the rGO sponge was considered as the combined resistance of identical unit components that were connected in series and parallel, as shown in Fig. 4 (a). We define a pair of multilayer rGO flakes as the unit component of G-0, as shown in Fig. 4 (b), and that of GDs will be explained later. This model was based on the assumptions that the sponge was homogenously composed of numerous rGO flakes and that the change in the resistance of the sponge at stretching was determined only by the change in contact resistance between rGO flakes, while the resistance of a single rGO flake remained constant. We employ the intrinsic resistance of a single rGO flake (R_i), the contact resistance between two rGO flakes at releasing (R_c), and the difference in the contact resistance at stretching (ΔR_c). The resistances of G-0 and GDs were denoted with suffixes, such as R_i(G-0) and R_i(GD). The R_i is determined by resistivity, cross-sectional area, and length of rGO flakes. As we assumed that the rGO flakes possessed the same resistivity and flake size, the R_i depends only on the rGO flake thickness. In our previous work,[34] the rGO flake thickness of G-0 is evaluated to be twice that of GDs (~10 nm and ~5 nm, respectively), suggesting that $2R_i$(G-0)=R_i(GD). Meanwhile, the R_c is determined by the contact area between two rGO flakes. The resistance of the unit component of G-0 at the initial state is $2R_i$(G-0)+R_c(G-0) (Fig. 4 (b)). Because the total amount of rGO was the same for G-0 and GDs and the thickness was half for GDs, the number of rGO flakes in GDs was twice that of G-0. Thus, we defined two pairs of rGO flakes connected in parallel as the unit component of GDs, as shown in Fig. 4 (c), so that the numbers of unit components were the same for G-0 and GDs. Accordingly, the resistance of the unit component of GDs at the initial state is expressed as $(2R_i$(GD)+R_c(GD))/2.

Based on the model, we explained the experimental result that the R_0 exhibited a similar value in G-0 and GDs. Because the rGO sponges, G-0 and GDs, were

isotopically composed of the same number of each unit component, their resistances R_0 were proportional to the resistances of the corresponding unit components. From the definitions of the unit components and the relation of $R_i(\text{G-0})$ and $R_i(\text{GD})$ as discussed above, the resistances of the unit components of G-0 and GDs can be expressed as $2R_i(\text{G-0})+R_c(\text{G-0})$ and $2R_i(\text{G-0})+R_c(\text{GD})/2$, respectively. Moreover, regarding R_c, our previous study[46] has revealed that the non-contact area and contact area of rGO flakes possess similar sheet resistance, which is consistent with other studies[47, 48]. This indicates that the R_c was much smaller than the R_i for the rGO flakes with high crystallinity and that the contribution of the R_c to the R_0 was negligibly small compared with that of the R_i. Consequently, the R_0 of both G-0 and GDs was approximated as $2R_i(\text{G-0})$, which can explain the comparable values of the R_0 for G-0 and GDs.
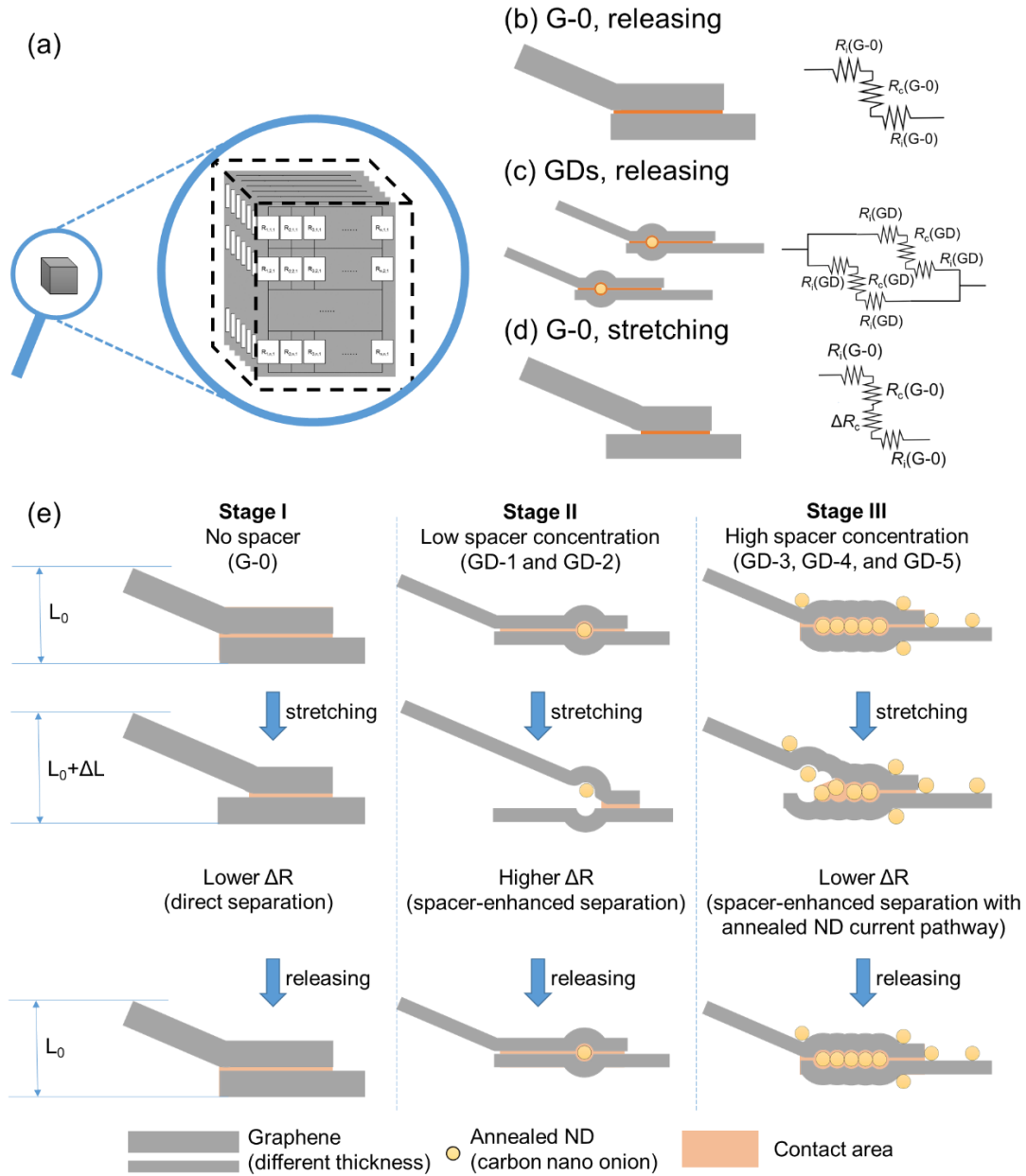
Fig. 4. (a) Schematic image of the model in which the rGO sponge is composed of unit components. (b–d) Schematic images of unit components of (b) G-0 when releasing $(2R_i(\text{G-0})+R_c)$, (c) GDs when releasing $(2R_i(\text{GD})+R_c)$, and (d) G-0 when stretching $(2R_i(\text{G-0})+R_c+\Delta R_c)$. (e) Schematic image showing the nanospacer effect in the strain sensor with increasing spacer concentration. There are three stages from left to right: a graphene sponge with no spacers, one with a lower spacer concentration, and one with a higher spacer concentration. The length of the strain sensors during stretching and releasing, L_0 and $L_0+\Delta L$, respectively, were shown on the left side.

14

We then discussed the variation of ΔR_{max} with the ND concentration based on the model. The resistance of the unit component of G-0 at stretching is expressed as $2R_i$(G-0)+R_c(G-0)+ΔR_c(G-0), as shown in Fig. 4 (d). Considering the change from the released state to the stretched state, ΔR_{max}(G-0) was proportional to $\Delta R_{c(G-0)}$ at the highest strain (length was $L_0+\Delta L$). Similarly, ΔR_{max}(GD) was proportional to ΔR_c(GD)/2. Thus, the ΔR_c with different ND concentration should be considered for explaining the trend of ΔR_{max}. In our experiment, the ΔR_{max} firstly reached a peak at a low spacer concentration, and then it decreased with further increasing spacer concentration (Fig. 3 (e)). Thus, the variation of ΔR_{max} was divided into three stages depending on the ND concentration, as shown in Fig. 4 (e). In stage I, the ΔR_c of the pure rGO sample (G-0) indicated a certain positive value because of the decreased contact area for the separation of the rGO flakes during stretching. In stage II, by adding a small amount of ND (GD-1 and GD-2), much higher ΔR_c was obtained after stretching than that of stage I. The steeper decrease in the contact area of the rGO flakes in GDs, than that of G-0, was attributed to the annealed ND, which can facilitate the separation of rGO flakes[40, 41]. Thus, the sample of stage II achieved the highest ΔR_c and accordingly the highest ΔR_{max} because of the low contact area and the least conductive path of annealed ND compared to those of other samples. In stage III, the ΔR_c decreased with further increasing the ND concentration. From the diameter of the annealed ND and the thickness of the rGO flakes, we calculated the occupation of the projected area of annealed ND on the rGO flake to be about 23% in GD-5, as shown in Fig. S4. The high occupation of the projected area by annealed ND (CNO), which was electrically conductive, can provide additional conductive paths, even between separated rGO flakes during stretching. This brought about decreases in ΔR_c and then in ΔR_{max} in stage III. Consequently, the ΔR_{max}

reached a peak at a low spacer concentration and decreased when the spacer concentration was further increased.

4. Conclusion

In this study, high linearity, small hysteresis, and low R_0 were achieved in the rGO strain sensor, by realizing the high crystallinity in the rGO sponge via ethanol-associated ultra-high temperature process. The R_0 decreased from 7.7 Ω to 2.25 Ω for the increase in the crystallinity. Then, the sensitivity of the strain sensor was further improved by the addition of ND, because the annealed ND can facilitate the separation of rGO flakes during stretching. After adding ND, the GF first increased from 3.7 (G-0) to 6.6 (GD-1), but it decreased to 4.4 (GD-5) for a further increase in ND concentration. The behavior of ΔR_{max} and R_0 of G-0 and GDs were understood by analyzing the R_i and the R_c under stretching or releasing based on the structural model. Accordingly, by increasing the crystallinity and adding a low concentration of ND, the strain sensor can achieve high linearity, small hysteresis, and low R_0, as well as improved GF, making it a promising candidate for future applications, such as human motion detection and automated logistics transportation.

Reference

1) H. Liu, H. Zhang, W. Han, H. Lin, R. Li, J. Zhu and W. Huang: Advanced Materials. **33** [8], 2004782 (2021).

2) W. Shen, R. Yan, L. Xu, G. Tang and X. Chen: Optik. **126** [17], 1499 (2015).

3) D. Maurya, S. Khaleghian, R. Sriramdas, P. Kumar, R.A. Kishore, M.G. Kang, V. Kumar, H.-C. Song, S.-Y. Lee and Y. Yan: Nature communications. **11** [1], 5392 (2020).

4) G. Ge, W. Huang, J. Shao and X. Dong: Journal of Semiconductors. **39** [1], 011012 (2018).

5) Y. Wang, L. Wang, T. Yang, X. Li, X. Zang, M. Zhu, K. Wang, D. Wu and H. Zhu: Advanced Functional Materials. **24** [29], 4666 (2014).

6) A. Qiu, P. Li, Z. Yang, Y. Yao, I. Lee and J. Ma: Advanced Functional Materials. **29** [17], 1806306 (2019).

7) J. Park, I. You, S. Shin and U. Jeong: ChemPhysChem. **16** [6], 1155 (2015).

8) M. Chao, Y. Wang, D. Ma, X. Wu, W. Zhang, L. Zhang and P. Wan: Nano Energy. **78**, 105187 (2020).

9) Y. Lu, M.C. Biswas, Z. Guo, J.-W. Jeon and E.K. Wujcik: Biosensors and bioelectronics. **123**, 167 (2019).

10) H. Hosseini, M. Kokabi and S.M. Mousavi: Polymer. **137**, 82 (2018).

11) X. Zhao, L. Xu, Q. Chen, Q. Peng, M. Yang, W. Zhao, Z. Lin, F. Xu, Y. Li and X. He: Advanced Materials Technologies. **4** [9], 1900443 (2019).

12) W. Obitayo and T. Liu: Journal of Sensors. **2012**, 652438 (2012).

13) Y. Cai, J. Shen, Z. Dai, X. Zang, Q. Dong, G. Guan, L.J. Li, W. Huang and X. Dong: Advanced Materials. **29** [31], 1606411 (2017).

14) P. Zhang, Y. Chen, Y. Li, Y. Zhang, J. Zhang and L. Huang: Sensors. **20** [4], 1154 (2020).

15) L. Lu, X. Wei, Y. Zhang, G. Zheng, K. Dai, C. Liu and C. Shen: Journal of Materials Chemistry C. **5** [28], 7035 (2017).

16) G.-S. Liu, F. Yang, J. Xu, Y. Kong, H. Zheng, L. Chen, Y. Chen, M.X. Wu, B.-R. Yang and Y. Luo: ACS Applied Materials & Interfaces. **12** [42], 47729 (2020).

17) Y. Gao, F. Guo, P. Cao, J. Liu, D. Li, J. Wu, N. Wang, Y. Su and Y. Zhao: Acs Nano. **14** [3], 3442 (2020).

18) Y.-J. Kim, J.Y. Cha, H. Ham, H. Huh, D.-S. So and I. Kang: Current Applied Physics. **11** [1], S350 (2011).

19) J. Lv, C. Kong, C. Yang, L. Yin, I. Jeerapan, F. Pu, X. Zhang, S. Yang and Z. Yang: Beilstein Journal of Nanotechnology. **10** [1], 475 (2019).

20) C. Lee, X. Wei, J.W. Kysar and J. Hone: Science. **321** [5887], 385 (2008).

21) Y. Wang, D. Lu, F. Wang, D. Zhang, J. Zhong, B. Liang, X. Gui and L. Sun: Carbon. **161**, 563 (2020).

22) T. Yang, X. Jiang, Y. Zhong, X. Zhao, S. Lin, J. Li, X. Li, J. Xu, Z. Li and H. Zhu: ACS Sens. **2** [7], 967 (2017).

23) C. Qian, T. Xiao, Y. Chen, N. Wang, B. Li and Y. Gao: Advanced Engineering Materials. **24** [4], 2101068 (2021).

24) Y. Liu, Q. Shi, C. Hou, Q. Zhang, Y. Li and H. Wang: Carbon. **125**, 352 (2017).

25) S. Chun, Y. Choi and W. Park: Carbon. **116**, 753 (2017).

26) A. Mehmood, N.M. Mubarak, M. Khalid, R. Walvekar, E.C. Abdullah, M.T.H. Siddiqui, H.A. Baloch, S. Nizamuddin and S. Mazari: Journal of Environmental Chemical Engineering. **8** [3], 103743 (2020).

27) F. Li, X. Jiang, J. Zhao and S. Zhang: Nano Energy. **16**, 488 (2015).

28) J. Huang, H. Wang, J.-a. Li, S. Zhang, H. Li, Z. Ma, M. Xin, K. Yan, W. Cheng, D. He, X. Wang, Y. Shi and L. Pan: ACS Materials Letters. **4** [11], 2261 (2022).

29) K.S. Novoselov, V.I. Fal'ko, L. Colombo, P.R. Gellert, M.G. Schwab and K. Kim: Nature. **490** [7419], 192 (2012).

30) Y.-G. Kim, J.-H. Song, S. Hong and S.-H. Ahn: npj Flexible Electronics. **6** [1], 52 (2022).

31) Y.V. Skrypnyk and V.M. Loktev: Physical Review B. **82** [8], 085436 (2010).

32) T.M. Radchenko, A.A. Shylau and I.V. Zozoulenko: Solid State Communications. **195**, 88 (2014).

33) Z. Xu, S. Nakamura, T. Inoue, Y. Nishina and Y. Kobayashi: Carbon. **185**, 368 (2021).

34) Z. Xu, T. Inoue, Y. Nishina and Y. Kobayashi: Journal of Applied Physics. **132** [17], 174305 (2022).

35) K. Uemura, T. Ikuta and K. Maehashi: Japanese Journal of Applied Physics. **57** [3], 030311 (2018).

36) R. Negishi, C. Wei, Y. Yao, Y. Ogawa, M. Akabori, Y. Kanai, K. Matsumoto, Y. Taniyasu and Y. Kobayashi: physica status solidi (b). **257** [2], 1900437 (2019).

37) I.I. Kulakova: Physics of the Solid State. **46** [4], 636 (2004).

38) X. Duan, Z. Ao, H. Zhang, M. Saunders, H. Sun, Z. Shao and S. Wang: Applied Catalysis B: Environmental. **222**, 176 (2018).

39) M. Zeiger, N. Jäckel, V.N. Mochalin and V. Presser: Journal of Materials Chemistry A. **4** [9], 3172 (2016).

40) F. Su, G. Chen and P. Huang: Friction. **8**, 47 (2020).

41) J. Xu, X. Chen, P. Grützmacher, A. Rosenkranz, J. Li, J. Jin, C. Zhang and J. Luo: ACS Applied Materials & Interfaces. **11** [28], 25535 (2019).

42) A. Vindhyasarumi, K.P. Anjali, A.S. Sethulekshmi, J. S Jayan, B.D.S. Deeraj, A. Saritha and K. Joseph: European Polymer Journal. **194**, 112143 (2023).

43) N. Morimoto, T. Kubo and Y. Nishina: Scientific Reports. **6** [1], 21715 (2016).

44) A.C. Ferrari and D.M. Basko: Nature Nanotechnology. **8** [4], 235 (2013).

45) K.N. Kudin, B. Ozbas, H.C. Schniepp, R.K. Prud'homme, I.A. Aksay and R. Car: Nano Letters. **8** [1], 36 (2008).

46) R. Negishi and Y. Kobayashi: Applied Physics Letters. **105** [25], 253502 (2014).

47) A.B. Kaiser, C. Gómez-Navarro, R.S. Sundaram, M. Burghard and K. Kern: Nano letters. **9** [5], 1787 (2009).

48) T. Kobayashi, N. Kimura, J. Chi, S. Hirata and D. Hobara: Small. **6** [11], 1210 (2010).

Supporting Information

Improved performance of strain sensors constructed by highly crystalline graphene with nanospacer

Zizhao Xu[1*], Yuna Himura[1], Chikako Ishiguro[1], Taiki Inoue[1], Yuta Nishina[2], Yoshihiro Kobayashi[1*]

[1]*Department of Applied Physics, Graduate School of Engineering, Osaka University,*

2-1 Yamadaoka, Suita, Osaka, 565-0871, Japan

[2]*Research Core for Interdisciplinary Sciences, Okayama University, 3-1-1 Tsushima-naka,*
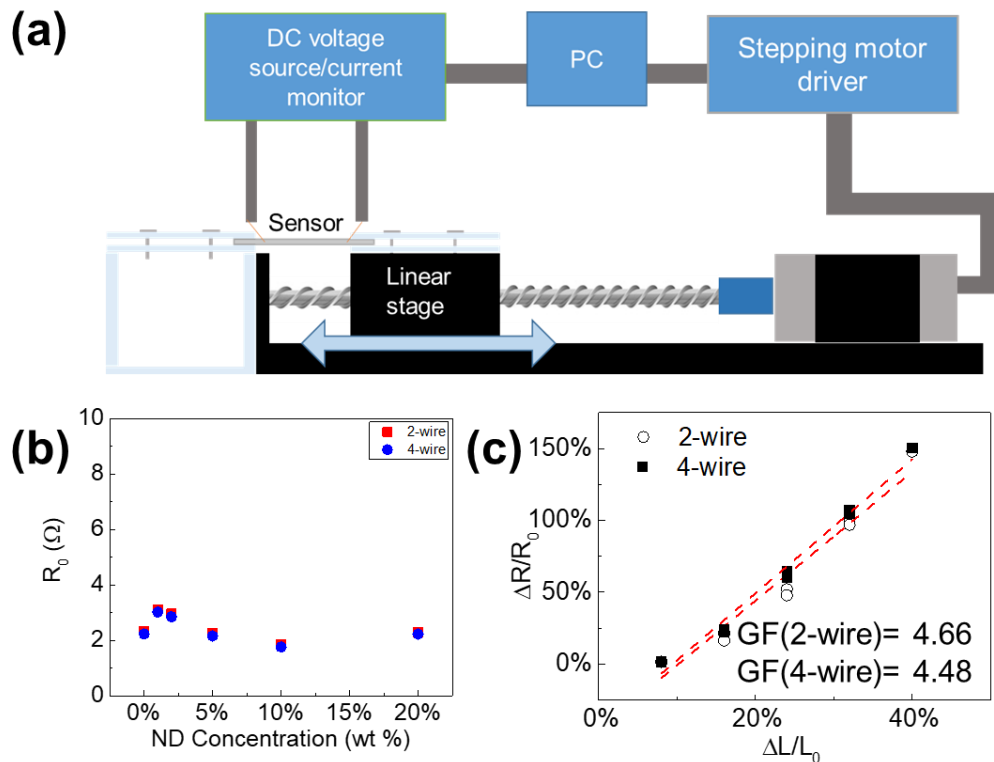
Kita-ku, Okayama, 700-8530, Japan

Figure S1 (a) Schematic image of lab-made measurement set-up for strain sensor, (b) the initial resistance obtained by the 2-wire and 4-wire methods, (c) Typical result of strain sensor performance testing, and the sensor performance obtained by the 2-wire and 4-wire methods.
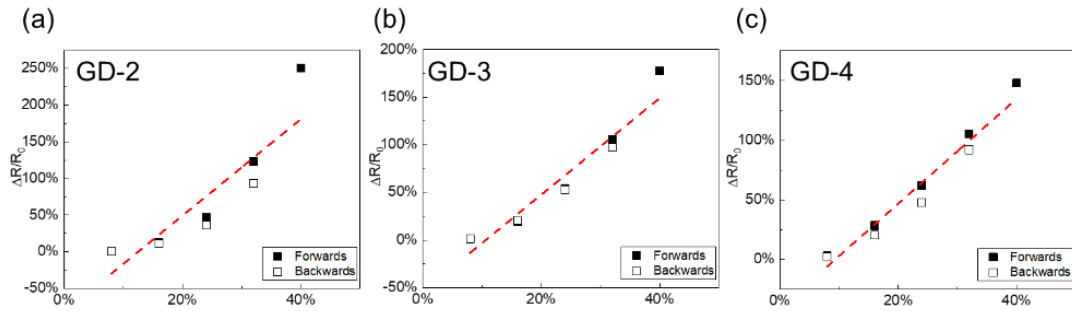
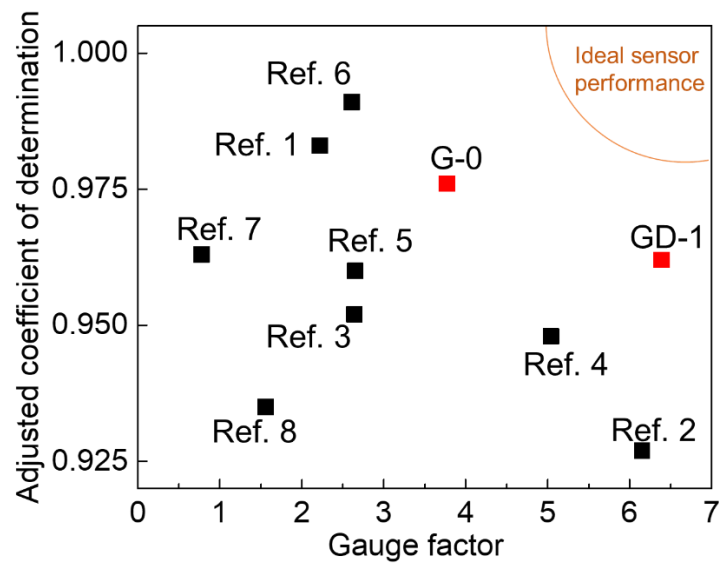Figure S2 Sensor performance of (a) GD-2, (b) GD-3, and (c) GD-4.

Figure S3 Other previous studies of linearity and sensitivity on graphene-based strain sensors.[1-8]
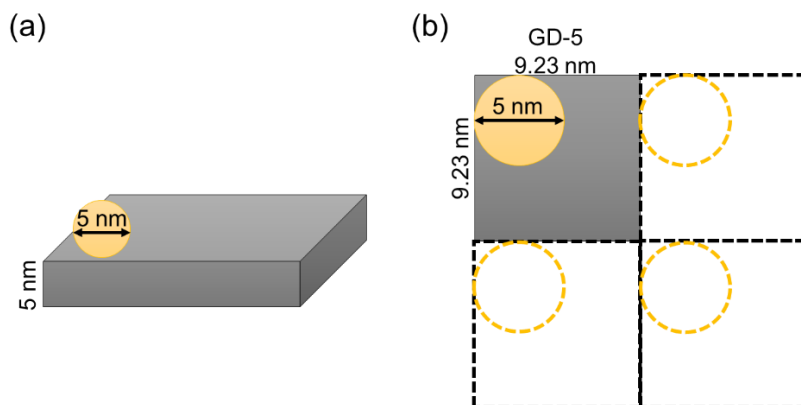

Figure S4 (a) The occupation of the projected area of annealed ND on the 5-nm-thickness rGO flake of GD-5. (b) The assumption of ND possessed a square lattice arrangement.

The GD-5 sample was prepared by incorporating 0.8 wt% of GO, 0.2 wt% ND, and 99% water.

For a 1-cm^3 sponge, the mass of ND (m(ND)) was 0.002 g, and the mass of GO (m(GO)) was 0.008 g. Considering the respective densities of GO (ρ(GO)) and ND (ρ(ND)), which are 0.00216 g/mm^3 and 0.00352 g/mm^3, the volumes of GO and ND can be calculated as follows:

$$V(GO) = 0.008/0.00216 = 3.70 \text{ mm}^3 = 3.7 \times 10^{36} \text{ nm}^3$$

$$V(ND) = 0.002/0.00352 = 0.568 \text{ mm}^3 = 0.568 \times 10^{36} \text{ nm}^3$$

For a single ND particle with a diameter of 5 nm, its volume (V(1-ND)) can be determined using the formula for the volume of a sphere:

$$V(1\text{-}ND) = 4/3 \times 3.14 \times 2.5^3 = 65.4 \text{ nm}^3$$

By dividing the V(ND) by the V(1-ND), the number of ND particles (n(ND)) in the sample can be calculated:

$$n(ND) = 0.568 \times 10^{36} \text{ nm}^3 / 65.4 \text{ nm}^3 = 8.69 \times 10^{33}$$

Next, the size of graphene, s(GO), with a thickness of 5 nm can be determined by dividing V(GO) by the thickness, as shown in S4 (a):

$$s(GO) = 3.70 \times 10^{36} \text{ nm}^3 / 5 \text{ nm} = 7.41 \times 10^{35} \text{ nm}^2$$

To calculate the area of graphene that accommodates a single ND particle, A(ND), the s(GO) is divided by the n(ND):

$$A(ND) = 7.41 \times 10^{35} \text{ nm}^2 / 8.69 \times 10^{33} = 85.3 \text{ nm}^2$$

Furthermore, assuming that the ND possessed a square lattice arrangement, the distance between two ND particles, d(ND), can be obtained by taking the square root of the A(ND), as shown in S4 (b):

$$d(ND) = \sqrt{85.3 \text{ nm}^2} = 9.23 \text{ nm}$$

Similarly, the d(ND) and the occupation of the projected area of annealed ND on the rGO flake for GD-1, GD-2, GD-3, GD-4, and GD-5 can be obtained as follows:

GD-1: 41.3 nm (1.2%)

GD-2: 29.2 nm (2.3%)

GD-3: 18.5 nm (5.7%)

GD-4: 13.1 nm (11.4%)

GD-5: 9.23 nm (23.0%)

Accordingly, the occupation of the projected area of annealed ND on the rGO flake was obtained.

Reference

1) Y. Cai, J. Shen, Z. Dai, X. Zang, Q. Dong, G. Guan, L.J. Li, W. Huang and X. Dong: Advanced Materials. **29** [31], 1606411 (2017).

2) Y. Pang, H. Tian, L. Tao, Y. Li, X. Wang, N. Deng, Y. Yang and T.-L. Ren: ACS Applied Materials & Interfaces. **8** [40], 26458 (2016).

3) C. Yan, J. Wang, W. Kang, M. Cui, X. Wang, C.Y. Foo, K.J. Chee and P.S. Lee: Advanced Materials. **26** [13], 2022 (2014).

4) Y.R. Jeong, H. Park, S.W. Jin, S.Y. Hong, S.-S. Lee and J.S. Ha: Advanced Functional Materials. **25** [27], 4228 (2015).

5) C. Xiong, M. Li, W. Zhao, C. Duan and Y. Ni: Journal of Materiomics. **6** [3], 523 (2020).

6) D. Du, P. Li and J. Ouyang: Journal of Materials Chemistry C. **4** [15], 3224 (2016).

7) H. Chen, L. Lv, J. Zhang, S. Zhang, P. Xu, C. Li, Z. Zhang, Y. Li, Y. Xu and J. Wang: Nanomaterials. **10** [2], 218 (2020).

8) S. Baloda, Z.A. Ansari, S. Singh and N. Gupta: IEEE Sensors Journal. **20** [22], 13302 (2020).